Publication Year	2020
Acceptance in OA	2025-02-11T17:24:07Z
Title	Infrared Observations of Ganymede From the Jovian InfraRed Auroral Mapper on Juno
Authors	MURA, Alessandro, ADRIANI, Alberto, SORDINI, Roberto, Sindoni, G., Plainaki, C., TOSI, Federico, FILACCHIONE, GIANRICO, Bolton, S., ZAMBON, Francesca, Hansen, C. J., CIARNIELLO, Mauro, Brooks, S., PICCIONI, GIUSEPPE, GRASSI, Davide, ALTIERI, FRANCESCA, MIGLIORINI, Alessandra, Moriconi, M. L., NOSCHESE, Raffaella, CICCHETTI, ANDREA
Publisher's version (DOI)	10.1029/2020JE006508
Handle	http://hdl.handle.net/20.500.12386/35908
Journal	JOURNAL OF GEOPHYSICAL RESEARCH (PLANETS)
Volume	125

JGR Planets

RESEARCH ARTICLE

10.1029/2020JE006508

Special Section:

Jupiter Midway Through the Juno Mission

Key Points:

- Water ice distribution for previously unmapped regions
- Latitudinal variability of CO_2 spectral feature
- New photometric model for Ganymede reflectance

Correspondence to:

A. Mura,
alessandro.mura@inaf.it

Citation:

Mura, A., Adriani, A., Sordini, R., Sindoni, G., Plainaki, C., Tosi, F., et al. (2020). Infrared observations of ganymede from Juno/Jovian infrared auroral mapper. *Journal of Geophysical Research: Planets*, *125*, e2020JE006508. https://doi.org/10.1029/2020JE006508

Received 3 MAY 2020
Accepted 26 OCT 2020

Infrared Observations of Ganymede From the Jovian InfraRed Auroral Mapper on Juno

A. Mura[1], A. Adriani[1], R. Sordini[1], G. Sindoni[2], C. Plainaki[2], F. Tosi[1], G. Filacchione[1], S. Bolton[3], F. Zambon[1], C. J. Hansen[4], M. Ciarniello[1], S. Brooks[5], G. Piccioni[1], D. Grassi[1], F. Altieri[1], A. Migliorini[1], M. L. Moriconi[6], R. Noschese[1], and A. Cicchetti[1]

[1]Istituto Nazionale di AstroFisica – Istituto di Astrofisica e Planetologia Spaziali (INAF-IAPS), Rome, Italy, [2]Agenzia Spaziale Italiana, Rome, Italy, [3]Space Science and Engineering Division, Southwest Research Institute, San Antonio, TX, USA, [4]Planetary Science Institute, Tucson, AZ, USA, [5]Jet Propulsion Laboratory, California Institute of Technology, Pasadena, CA, USA, [6]CNR-Istituto di Scienze dell'Atmosfera e del Clima, Rome, Italy

Abstract The Jovian InfraRed Auroral Mapper (JIRAM) on board the NASA Juno spacecraft is a dual-band imager and spectrometer in the 2–5 μm range with 9-nm spectral sampling, primarily designed to study the Jovian atmosphere and aurorae. In addition to these goals, JIRAM is used to obtain images and spectra of the Galilean satellites, every time the spacecraft attitude is favorable. Here we present JIRAM images and spectra of Ganymede obtained during the first 4 years of the mission. In particular, on 26 December 2019, during a relatively close passage of Juno with the moon, a dedicated reorientation of the spacecraft was performed to achieve optimized observations of Ganymede by Juno's remote sensing instruments, including JIRAM. In the outbound phase of the flyby, observing the northern polar regions of Ganymede at a distance of roughly 100,000 km, JIRAM collected infrared images and spectra of the surface at a spatial resolution as high as 23 km per pixel, covering high northern latitudes that were scarcely mapped previously. A photometric model of Ganymede reflectance is produced, which diverges from the Lambert model. The spatial distribution of the obtained spectra complements the available coverage of the surface, with particular regard to the 2.0-μm water ice absorption band and, to a lesser extent, to the 4.26-μm spectral feature diagnostic of CO_2 trapped in water ice. The water ice distribution is compatible with sputtered-induced water ice grain enrichment at high latitude (>45°). Several minor species (hydrated salts, trapped H_2, CO_2, and acids) are also identified in the measured spectra.

Plain Language Summary The Jovian Infrared Auroral Mapper (JIRAM) is a dual-band imager and spectrometer on the NASA Juno spacecraft. It works in the range of 2–5 μm and its spectral sampling is 9 nm. JIRAM is mainly used to study the Jovian atmosphere and aurora. JIRAM is also used to obtain images and spectra of the moons of Jupiter, every time the spacecraft has a favorable attitude. Here, we show Ganymede images and spectra obtained during the first 4 years of the mission. On 26 December 2019, during a close passage of Juno to Ganymede, JIRAM observed it at a distance of approximately 100,000 km. In this occasion, JIRAM collected infrared images and surface spectra with a spatial resolution of up to 23 km per pixel. This data covers North polar regions that were not mapped before. A photometric model of Ganymede's reflectance was produced, and it is different from the Lambert model. The spatial distribution of the obtained spectrum can supplement the available coverage of the surface, especially for the 2.0 μm water ice absorption band. At high latitudes (>45°), the distribution of water ice is compatible with the enrichment of water ice particles induced by sputtering. Several minor species (hydrated salts, trapped H_2, CO_2, and acids) were also identified in the measured spectra.

1. Introduction

The largest Galilean moon of Jupiter, Ganymede, is in many aspects one of the most interesting objects in the solar system. Among its unique characteristics, we note that it is the largest object without a substantial atmosphere, the largest of all the satellites, and the only known one to possess an intrinsic magnetic field (Kivelson et al., 1996). It also has the lowest moment of inertia among planetary satellites, which is indicative of a substantial degree of differentiation.

With the exception of flyby observations made by Pioneer and Voyager missions, the first spacecraft to study Ganymede was NASA/Galileo (Johnson et al., 1992). With regards to the knowledge of the surface and interior of Ganymede, striking results were obtained by the on board magnetometer, the solid-state imaging camera, the near-infrared mapping spectrometer (NIMS), and the radio science experiment. In fact, our current knowledge of Ganymede still largely relies on results obtained by the Galileo instrument payload. From hyperspectral images returned by NIMS (Carlson et al., 1992), operating in the range 0.7–5.2 μm and with an average spectral sampling of 25 nm longward of 1 μm, we know that the satellite's surface composition is dominated by a mixture of water ices, trapped carbon dioxide (CO_2) and nonicy materials (Carlson et al., 1996; Hansen & McCord, 2004; McCord et al., 2001; McCord et al., 2001). Ganymede's water ice particles are generally smaller on the leading hemisphere than on the trailing hemisphere (Calvin et al., 1995), which is probably the result of micrometeorite gardening combined with sputtering effects on the trailing side. Furthermore, their size substantially decreases while moving away from the equatorial region to the poles (Stephan et al., 2020), as a result of increasing radiolytic fluxes and sputtering.

The sputtered ice particles can reach the polar regions and form a thin layer of frost (Khurana et al., 2007). Such material covers the polar regions and shows a higher albedo in the visible part of the spectrum. It has also been suggested by Hansen and McCord (2004), that such interaction with the Jovian magnetosphere may cause spectral differences with respect to the crystallinity and particle size of H_2O ice; in particular, with more crystalline ice at low latitudes and more amorphous ice in the polar regions. This may be caused by the configuration of Ganymede's own magnetic field that at least partly protects surface regions between ±40° latitude from impacting magnetospheric particles. However, it should also be noted that these studies were completed before good optical constants of amorphous and crystalline ices were available (Mastrapa et al., 2008, 2009), so that the evidence for amorphous ice is weaker.

NIMS also revealed spectral signatures centered at 3.4, 3.88, 4.05, and 4.26 μm on both Callisto and Ganymede—respectively interpreted as the C-H bond in tholins, the S-H bond (possibly due to SO_2-H_2S mixtures), sulfur dioxide (SO_2), and CO_2 that are found in cometary nuclei or that form by the action of charged particles impacting the icy surfaces (McCord et al., 1997, 1998). All of these features are weaker on Ganymede than on Callisto.

Non-water-ice materials have been interpreted as two different possible endmembers: in McCord et al. (1998, 1999) they were identified as hydrated salts thanks to their low reflectance at wavelengths shortward of 3 μm, subdued and especially asymmetric (distorted) water ice bands at 1.5 and 2.0 μm, and relatively high reflectance in the 3–5 μm range compared to H_2O ice; more recently, Carlson et al () have alternatively explained these spectral structure as the result of sulfuric acid hydration.

These spectral features were found locally associated with some dark features on Ganymede and also were interpreted as hydrated minerals similar to those suggested to exist on Europa (McCord et al., 2001). According to Hibbitts et al. (2003,) CO_2 appears to be most correlated with the moderately hydrated and nonicy material, which is primarily associated with the dark regions; there is no leading/trailing hemisphere asymmetry in the distribution of CO_2, nor do impact craters tend to be enriched in CO_2. Instead, they note that CO_2 is occasionally more abundant in areas containing larger grained ice than in adjacent areas of similar morphology and ice abundance.

The surface morphology of Ganymede indicates that it has experienced some endogenic activity (Pappalardo et al., 2004, and references therein). It is believed that the interior of Ganymede is differentiated into four layers: an iron core, a silicate mantle, a water ice-liquid shell and an icy crustal layer (McCord et al., 2001; Schubert et al., 2004). Near-infrared spectroscopic observations of Ganymede started as early as the 1960s. Reports of the discovery of water ice absorption (Kuiper, 1957, 1961; Moroz, 1965), and summaries of the first decades of spectroscopic observations can be found in Pollack et al., (1978), Clark and McCord, (1980), Calvin et al. (1995). Further space observations of Ganymede at infrared wavelengths were achieved by Cassini-Visual and Infrared Mapping Spectrometer (VIMS) (McCord et al., 2004) and New Horizons-LEISA (Grundy et al., 2007) during their flybys of Jupiter.

The surface of Ganymede is mostly made of water ice (Kieffer & Smythe, 1974; Sill & Clark, 1982), and exhibits spectrophotometric variability with the presence of dark and bright features. These features were first discussed by Smith et al. (1979) based on Voyager observations, then by Khurana et al. (2007) based on Galileo imagery, who explain the presence of observed bright polar caps on Ganymede with sputter-induced redistribution and subsequent cold trapping of water molecules.

Sputtering of Ganymede's icy surface, depending on the impacting ion energy, can take place only in those regions where Jupiter's magnetospheric plasma has access (i.e., outside the equatorial region). In particular, Khurana et al. (2007) noted a close correspondence between the open-closed field line boundary (OCFL) and the boundary of Ganymede's polar cap, which they interpreted as evidence that the latter is associated with charged particle effects.

Water ice can be either in crystalline or amorphous form on the surface of Ganymede. According to Hansen and McCord, (2004), who studied the properties of the Fresnel reflection peak at 3.1 μm, both crystalline and amorphous forms coexist. The former phase is enriched by thermal cycling, the latter due to plasma bombardment. Hence, while water ices are ubiquitous over the surface of Ganymede, they suggest that the crystalline phase is predominant at low latitudes and amorphous phase is more abundant at high latitudes, in the bright polar caps. As mentioned above, more recent laboratory measurements of the optical constants of amorphous and crystalline ices (Mastrapa et al., 2008, 2009), suggests reconsideration of the evidence for amorphous ice in Hansen and McCord (2004).

It was also suggested that the equatorial leading/trailing asymmetry was due to the preferential flux of ions onto Ganymede's leading hemisphere due to magnetotail reconnection. Simulations of both energetic ion precipitation on Ganymede's surface and sputter-induced exosphere generation (e.g., Jia et al., 2009; Plainaki et al., 2015; Poppe et al., 2018) seem to support such a scenario, with respect to both points. Indeed, simulations by Plainaki et al. (2015) and Poppe et al. (2018) show a shielded region close to Ganymede (at distances < 1.5 Ganymede radii, R_G) asymmetrically displaced toward the pro-Jovian, trailing hemisphere, enhancements of lower-energy ion flux along the trailing-side boundaries of Ganymede's Alfvén wings, and enhancements in the flux on the antiJovian, leading hemisphere (Poppe et al., 2018). It is worth noting, however, that current models depend significantly on a series of physical parameter assumptions (i.e., Ganymede's magnetic field and magnetosphere morphology, see for instance Paty et al., 2008 and Jia et al., 2009), the ice composition and sputtering yields) which are currently poorly known, mainly due to the absence of an adequate quantity of in situ and laboratory data. For this reason, and despite numerous modeling efforts (e.g., Leblanc et al., 2017; Plainaki et al., 2018; Poppe et al., 2018), we do not yet have the necessary information to disentangle the influence of different mechanisms on the spectral properties of Ganymede's surface; for example, the model by Plainaki et al. (2015) suggested different alternative explanations considering the ion circulation in Ganymede's magnetosphere, based on different assumptions.

In this study we discuss the observations by Jovian InfraRed Auroral Mapper (JIRAM) during the first 3 years of the Juno mission, and in particular those performed on 26 December 2019 (Juno's orbit 24), when JIRAM had a unique opportunity to observe Ganymede from a distance of ∼100,000 km, close enough to achieve broad regional coverage, both with its imager and its spectrometer, of the northern hemisphere with a spatial resolution as high as ∼25 km/pixel. To achieve this goal, the spacecraft needed to be substantially reoriented with respect to the nominal attitude.

2. Instrumentation and Data Set

The JIRAM (Adriani et al., 2008, 2014, 2016) is an imaging spectrometer on board the Juno spacecraft, whose observations of Jupiter began in July 2016 (Bolton et al., 2017). The instrument is comprised of an imager channel and a spectrometer channel, sharing the optics (a modified-Schmidt telescope).

The imager channel is a single detector (266 × 432 pixels), above which two different filters are placed. Of the two filters, the first (*L,* bandpass from 3.3 to 3.6 μm) is optimized to detect the H_3^+ auroral emission from Jupiter, while the second (*M,* bandpass from 4.5 to 5 μm) is suitable for mapping the thermal structures of the deep atmosphere. When looking at Ganymede, both the L- and M-band filters would mostly image the reflected sunlight from the surface. For both, the angular resolution per pixel (IFOV) is 237 μrad. Hence, the field of view (FOV) of both the L and M bands is 5.87° by 1.74°. The responsivity of the imager channel is 2×10^6 DN/(W m^{-2} sr^{-1} s^{-1}).

Table 1
List of Observations of the Imager and the Spectrometer Used for This Study

Orbit	Start UTC	Stop UTC	Surface resolution (km)	Number of spectra	Number of images	SSP longitude	SSP latitude	SSP SZA
6	2017/05/18 11:31:55	2017/05/18 13:30:10	~100	1,400	164	127 W	79 N	92
8	2017/09/02 20:42:14	2017/09/02 22:42:45	~200	883	1S80	56 W	79 S	91
10	2017/12/16 15:25:35	2017/12/16 16:08:00	~300	243	25	12 W	53 S	90
11	2018/02/07 22:23:49	2018/02/07 23:40:04	~200	459	119	−61 W	54 S	96
13 (*)	2018/05/23 16:52:26	2018/05/25 12:33:06	~300	833	449			
16	2018/10/30 12:09:42	2018/10/30 13:36:38	~200	230	148	69 W	58 S	90
18	2019/02/12 14:31:16	2019/02/12 15:16:25	~250	1,069	91	78 W	44 S	89
19	2019/04/06 00:34:18	2019/04/06 02:43:29	~150	4,105	239	39 W	23 S	96
21	2019/07/20 16:07:07	2019/07/20 17:26:22	~200	405	114	70W	24 S	95
24	2019/12/26 01:39:04	2019/12/26 16:21:24	~25	20,100	297	−60 W	64 N	81

Note. Distance, SSP longitude and latitude refer to the middle of the observation period. *Orbit 13 actually includes two different observations, one inbound and one outbound.

Abbreviation: SSP, sub-spacecraft point; SZA, solar zenith angle.

The spectrometer channel makes use of Littrow gratings to simultaneously acquire 256 contiguous spectra along the slit direction which has a one-dimensional FOV of 3.52°. It is co-located within the M-band filter FOV. Each spectrum covers the 2–5 μm spectral range sampled by 336 bands corresponding to an effective sampling of 9 nm/band.

Although observation of the Galilean moons is not a primary objective of the mission, the orbit of Juno provides frequent observation opportunities for them; JIRAM is used to collect infrared images and spectra of their surfaces every time this is possible. Previous works describe similar opportunities that were exploited to obtain observations of Europa and Io (Filacchione et al., 2019; Mura et al., 2020a, 2020b; Tosi et al., 2020). Between 31 July 2016 and 26 December 2019, Ganymede has been observed by JIRAM a total of 2,859 times over 11 different orbits, including 2,202 times with its imager and 657 times with its spectrometer, and with resolution ranging between 2,063 and 23 km/pixel (with a median value of 206 km/px, see Table 1).

Once per spacecraft rotation (~30 s), JIRAM acquires two 2D images in L-M spectral ranges and a 1D slit with full spectral resolution. A dedicated despinning mirror is placed at the telescope entrance to compensate for the spacecraft rotation (~12°/s). Differently from other imaging spectrometers, JIRAM cannot acquire contiguous spectra on the surface of Ganymede, because of the low acquisition rate mentioned above, and of Juno's high relative velocity with respect to the moon. Hence, the ground footprints of the spectrometer's slit are typically sparse across Ganymede's surface, but repeated observations can ultimately fill gaps and allow a substantial improvement in coverage, at the expense of some redundancy.

Geometric information associated with each JIRAM observation is obtained by using SPICE/Navigation and Ancillary Information Facility routines and ancillary data (Acton, 1996).

The JIRAM instrument is body-fixed to the spacecraft and is incapable of being articulated. However, by varying the timing of data acquisition, the JIRAM instrument can obtain data anywhere within a 360-degree range along the spacecraft spin plane. Obtaining data perpendicular to this plane requires a reorientation of the spacecraft spin axis. For this reason, to allow the observations of Ganymede during orbit 24, Juno was commanded to perform a ~60 degrees turn off the nominal pointing, in which Juno's solar arrays are oriented toward the sun, for about 3 h.

During Juno's orbit 24, on 26 December 2019 at 01:46 UTC, JIRAM started to collect images and spectra of Ganymede in the inbound phase from a distance of about 100,000 km above the surface, reaching a closest approach (C/A) at 02:12 UTC and then continuing to observe Ganymede in the outbound phase until 04:08 UTC. The surface pixel resolution varied from a minimum of 23 km/px to a maximum of 39 km/px. The

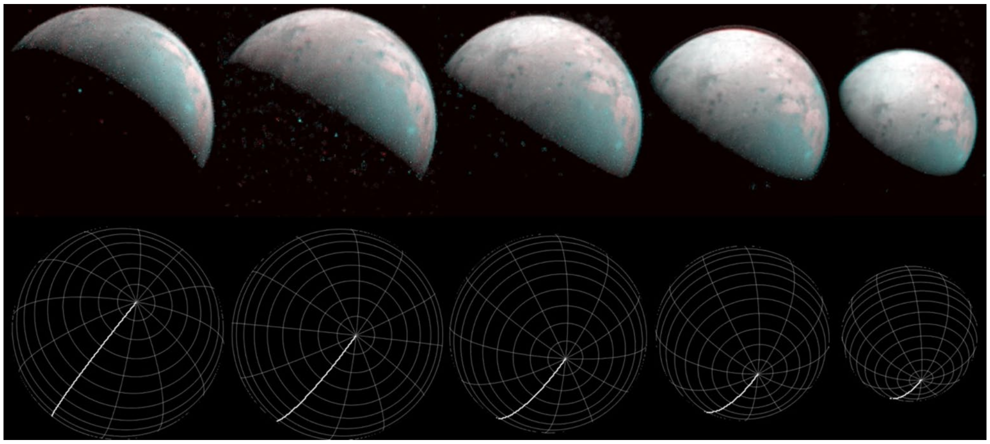

Figure 1. Top panels: five composite RGB images of Ganymede taken during PJ24 on 26 December 2019. Each image is made by combining all images from the same scan (up to 10 images) to form a superresolution image as in Mura et al. (2020b). Then the composite L-band image is used for the blue channel and the M-band image is used for the red channel. The green channel is given by the average of the two bands. UTCs are, from left to right 02.00.27 to 02.02.28, 02.27.09 to 02.30.41, 02.51.21 to 02.54.52, 03.18.34 to 03.23.06, and 04.04.26 to 04.08.59. Bottom panels: viewing geometry for the observations in the five cases. Meridians are every 30°, parallels are every 10°; thick line is 180°W.

subspacecraft point increased from 63°N at the beginning of the observations up to 80°N soon after the C/A point, before subsequently decreasing to 46°N. During this ~2.5 h period, JIRAM acquired a total of ~220 infrared images and 210 spectrometer acquisitions containing about 20,000 individual infrared spectra of the surface of Ganymede. The JIRAM FOV was tilted above and below the satellite to allow the spectrometer's slit to point to different locations on the surface, thus performing a scan of ~10 acquisitions (this is the usual observing strategy for all JIRAM sessions). Hence, most of the images cover Ganymede's surface only partially. In Figure 1, we show a panel with selected images taken during the flyby of Ganymede. A few minutes after the end of the observations, Ganymede entered into eclipse. However, with an off-Sun attitude of ~60°, the solar array power production was reduced by roughly a half compared to the nominal value. To avoid draining the spacecraft battery below acceptable engineering limits, the spacecraft was required to return to its nominal power-optimized orientation after roughly 2 h, precluding any observations of the eclipse itself.

3. Integrated Spectra and I/F

Here we start discussing the spectral analysis of the data. The first step involves calculating the radiance factor I/F, which is defined by Hapke et al. (1993), as "the reflectance relative to a perfect Lambert surface perpendicularly illuminated." In our study, JIRAM spectra are divided by the high-resolution MODTRAN extra-terrestrial solar irradiance based on combinations of measured and modeled data from multiple sources (Kurucz, 1995, 2005), taking into account the actual distance of Ganymede from the Sun. We note that a more recent reference spectrum (Thompson et al., 2015) does not differ significantly on average but has more detail, and may be preferably used in future studies. Given the large number of spectra, we present the results in term of orbit-averaged I/F. In the case of JIRAM data, spectral slits are not uniformly distributed on the target surface, nor do they cover it completely. Hence, the average I/F is not perfectly indicative of the actual total radiance as seen from the spacecraft, and there are scaling factors that depend on the actual distribution of the spectra on the surface, with varying incidence and emission angles. Also, the observation geometry varies slightly during the observation. In order to partially correct this effect, spectra variability may be corrected by applying a Lambert photometric model for those surface elements that are not illuminated perpendicularly, and a corrected I/F$_c$ is obtained. In the limit of applicability of the Lambert model (which in fact is discussed in Section 5), the obtained quantity is a spectral reflectance and hence can be compared to the values given in Spencer (1986). In Figure 2, we show the full-range computed I/F$_c$ from the dayside as observed in some selected orbits (orbits 10, 18, and 21 were noisy and are not shown but still

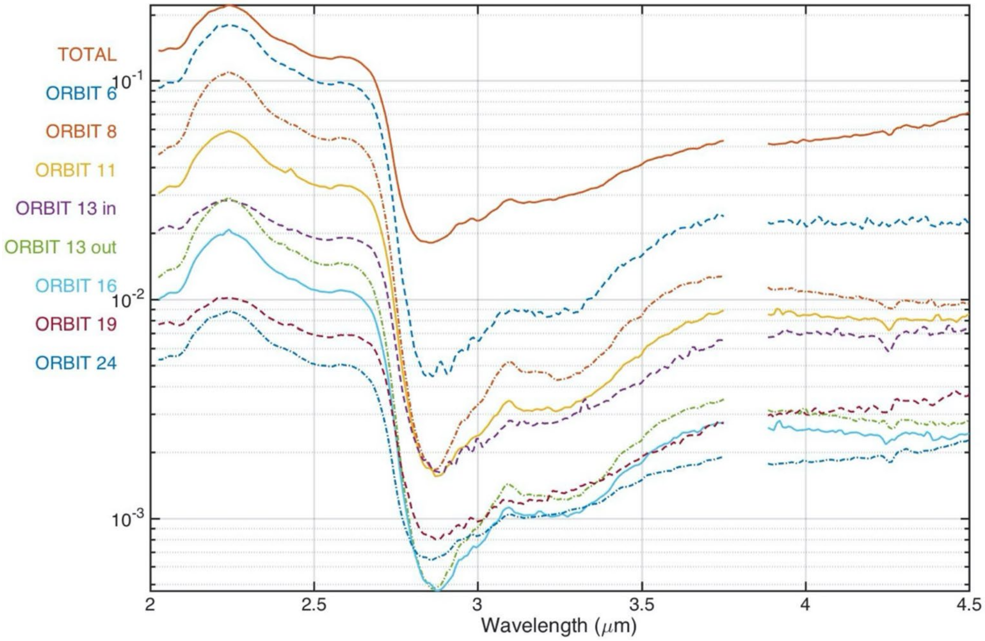

Figure 2. Dayside I/F computed for single orbits and for all orbits together; see text for details. The missing data at 3.8 μm is caused by a calibration residual of the instrumental order sorting filters junction, and it is intentionally removed. Data is presented in logarithmic scale; global I/F is plotted without offset; I/F for single orbits are plotted with an offset of a factor 2.

contribute to the estimation of the average I/F_c), while in Figure 3, we show the I/F calculated by averaging over all spectra from the illuminated side of Ganymede, for selected wavelength ranges.

The in-flight noise equivalent spectral radiance (NESR) of the spectrometer typically varies between 10^{-4} W/(m^2 sr μm) and 10^{-3} W/(m^2 sr μm). While computing an average spectrum, the standard deviation can be estimated as $NESR / \sqrt{n}$, where n is the number of independent spectra. After converting this value to I/F, it turns out that the standard deviation of the I/F is negligible with respect to systematic errors, the most important being the odd-even effect. This high frequency noise occurrs between odd and even spectral bands and is introduced by the detector's multiplexer (Filacchione et al., 2019); even bands register about 3% digital counts more than the odd ones, but such behavior depends on variables such as the temperature or the signal intensity. Hence, to suppress this noise, we smooth the spectra with a boxcar filter (two bands). The spectral resolution is hence increased to 18 nm, while the average spectral sampling is still 9 nm.

While the 2–5 μm spectra of Europa (Filacchione et al., 2019) and Io (Mura et al., 2020a, 2020b; Tosi et al., 2020) taken by JIRAM reveal several intense spectral signatures, infrared spectra of Ganymede are dominated by few recurrent features, for example, the 2 μm band (distorted by nonicy materials), the 3.1 μm Fresnel peak both assigned to water ice and the 4.25 μm band of CO_2, although fainter features can be identified after more accurate analysis reported in Section 4. Ganymede's spectra as observed by JIRAM on the dayside are dominated by solar reflection; any thermal characterization of the surface is complicated by the limited spectral range (2–5 μm) combined with the low surface temperature of Ganymede on its dayside, so it is not attempted here. The most prominent spectral feature is the absorption band of water ice centered at 2 μm, which has been discussed in the Introduction and whose band depth varies over Ganymede's surface. To map crystalline versus amorphous water ice based on near-infrared spectra, one needs to measure three diagnostic spectral indices: the depth of the 1.65-μm band, the shape and center of the 2.0-μm band, and the strength and shape of the 3.1-μm reflectance peak coming from the Fresnel reflection off the facets of the water ice grains on the surface (e.g., Grasset et al., 2017; Mastrapa et al., 2009). Unfortunately, the 1.65-μm feature is out of the JIRAM range of sensitivity, while only half of the 2.0-μm band is seen, ruling out the possibility of using these two features. Moreover, the 2 μm band appears distorted by the presence of non icy materials, like hydrated salts or acids, making it difficult to compare with a pure water ice band shape.

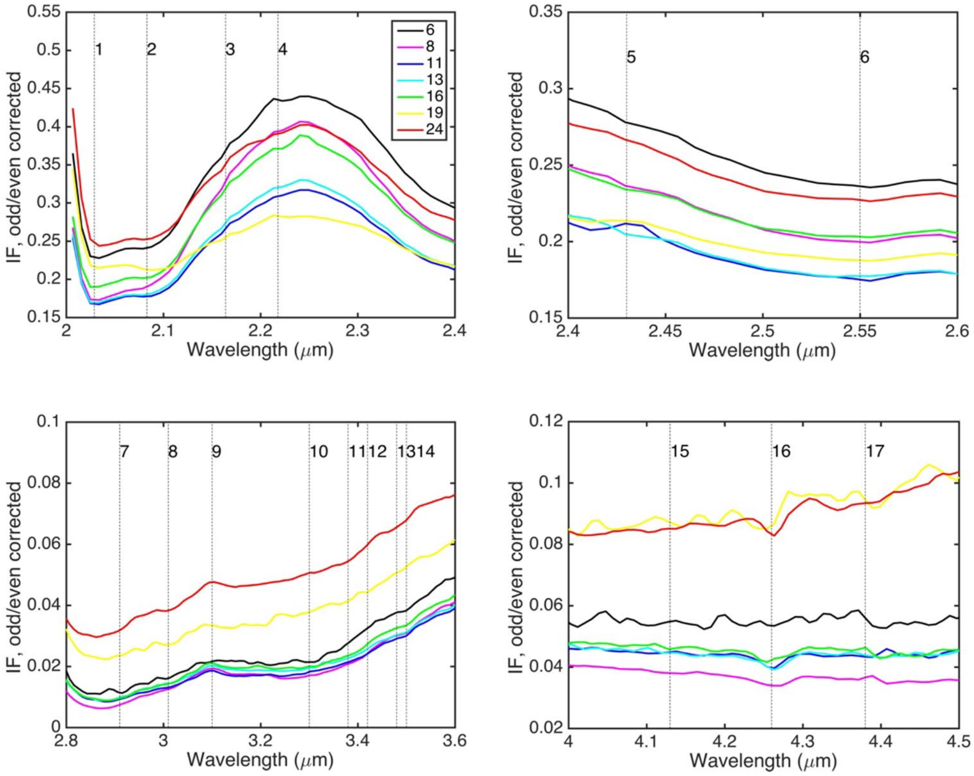

Figure 3. Spectral features identified on average I/F spectra of Ganymede during orbits 6 to 24. The features marked from 1 to 17 in the four panels are discussed in the text. No photometric correction has been applied. Odd even correction according to Filacchione et al. (2019) (Equation 1)

At about 2.5 μm another large absorption band is present; in this case, evaluating the band depth is more challenging because it is difficult to assess the continuum level. However, the 3.1-μm Fresnel peak nicely shows up in our I/F$_c$ spectral profiles, as does the asymmetry of this feature in specific cases (e.g., in orbit 8), which opens the possibility of future investigations of the relative amorphous/crystalline ice abundance using this feature.

On Ganymede, CO_2 is the most abundant volatile compound after H_2O. An absorption band diagnostic of CO_2 and centered at 4.26 μm is actually observed in most I/F profiles. Mapping this feature is not feasible without complex data processing, because the signal-to-noise ratio (SNR) in individual spectra is usually low at that wavelength. However, dividing the spectra into high and low latitude datasets, then binning and averaging the data is a good way to limit SNR issues, which is discussed in Section 6. Finally, the spectral profiles measured by JIRAM show inflections occurring within the main 3-μm water ice band, particularly in the region between 3.2 and 3.5 μm, which could be ascribed to organic compounds previously suggested on the basis of Galileo/NIMS data (McCord et al., 1997, 1998), but whose characterization is beyond the scope of our work. Instead, in JIRAM data of Ganymede there is no clear evidence of the 4.55-μm diagnostic signature of tholins or nitrile compounds. All the spectral features are discussed in details in the following section.

4. Spectral Analysis

The JIRAM dataset evidences a richness of spectral features visible on Ganymede average spectra collected during orbits 6 to 24. We focus in particular on the four spectral ranges 2.0–2.4, 2.4–2.6, 2.8–3.6, and 4.0–4.5 μm shown in Figure 3. In these spectra we recognize the presence of 17 signatures and discuss possible attributions to each of them.

At around 2 μm, all JIRAM observations show the presence of the strong water ice band, distorted by the presence of contaminants. In fact, for pure water ice one would expect a single minimum between 2.017 μm (at a temperature of 120 K) to 2.001 μm (at 150 K) for the crystalline form and at approximately 2.0 μm for the amorphous one (Mastrapa et al., 2008).

Note, however, that Clark et al., (2012) revised the optical constants by Mastrapa et al. (2008, 2009). Clark et al. (2012) show the Fresnel peak position and shape changes significantly in reflectance between amorphous and crystalline ice (their Figure 12), and that the Fresnel peak decreases with grain size and is suppressed with particles, including contaminants, smaller than 1 μm. Clark et al. also showed that diffraction from small particles (either small ice grains or contaminants) distort the shape and position of ice spectral features observed in reflectance. For example, crystalline ice shows a reflectance maximum near 2.53 μm but amorphous ice does not (Cruikshank et al., 2020). But Clark et al. shows that small particle also suppress that peak in crystalline ice. Our spectra (Figure 2) shows this peak, thus indicating crystalline ice and low abundance of submicron particles. The 2-μm ice band in reflectance shifts shorter for amorphous ice and longer in crystalline ice with submicron grains, and both show show changes relative to reflectance of crystalline ice with grain sizes greater than about 1 μm (Clark et al., 2012; Cruikshank et al., 2020). Our spectra of Ganymede are inconsistent with amorphous ice (Figure 3) as the band minimum is longer than 2 μm, although the position is also influenced by nonice components. But all the data, from 3.1-μm Fresnel peak, 2.5-μm region, and 2-μm absorption are more consistent with crystalline ice than amorphous ice.

On Ganymede we observe a more structured band shape with at least two minima at 2.029 μm (feature A1) and at 2.083 μm (A2) common to many spectra, with the center of the feature shifted systematically toward longer wavelengths with respect to pure water ice. The feature A2 is shifted toward 2.1 μm on more contaminated spectra, such as on orbit 19. The presence of two minima within the broad feature resembles the absorption structures of magnesium-rich hydrated salts: $MgSO_4 \cdot 6H_2O$ at temperature of 93 K has two minima at 2.010 and 2.060 μm (De Angelis et al., 2017); $MgSO_4 \cdot 7H_2O$ (at 93 K) has minima at 2.000 and 2.060 μm (De Angelis et al., 2017); $Na_2Mg\,(SO_4)_2 \cdot 4(H_2O)$ shows absorptions at 2.000 and 2.100 μm (Dalton and Pitman, 2012). Apart from water ice and salts, even CO_2 could also contribute to the overall band shape since it is characterized by a narrow triplet absorption at 1.966, 2.012, and 2.070 μm (Quirico et al., 1999; Quirico & Schmitt, 1997; White et al., 2012), the longer wavelength component of which approximately corresponds with feature A2 in JIRAM spectra. Conversely, the presence of stray light in the first three bands of JIRAM makes the identification of the CO_2 triplet central feature uncertain.

Moving toward the long-wavelength shoulder of the wide 2 μm band we observe other two signatures at 2.164 μm (A3) and at 2.218 μm (A4): both are compatible with laboratory spectra of $MgSO_4 \cdot 6H_2O$, which has an absorption at 2.120 and 2.200 μm (De Angelis et al., 2017), while the latter could also be compatible also with a signature of $Na_2Mg\,(SO_4)_2 \cdot 4(H_2O)$ measured at 2.270 μm (Dalton and Pitman, 2012). We note that the vibrational modes of hydrated salts are strongly dependent on temperature and hydration: these effects could explain the small mismatch between the wavelengths of the absorption features in JIRAM observations and laboratory measurements.

In the 2.4–2.6 μm range, shown in panel B, two shallow signatures are recognizable: B5 at 2.430 μm is compatible with trapped H_2, a radiation product from destruction of H_2O (Clark et al., 2008, 2012) or with $Na_2Mg\,(SO_4)_2.4(H_2O)$ hydrated salt (Dalton and Pitman, 2012). The B5 feature is recurrent across the JIRAM dataset with the exception of orbits #11 and 19 where a local bump is observed.

B6 at 2.550 μm could be compatible with both $MgSO_4 \cdot 6H_2O$ (93K) and $MgSO_4 \cdot 7H_2O$ (93K) absorption at 2.500 μm (De Angelis et al., 2017).

The spectral range between 2.8 and 3.6 μm (panel C) is characterized by the presence of seven signatures (C7–C13). Feature C7 (2.910 μm), recognizable on orbits 6 and 19, could be caused by instrumental noise or by NH_3 ice (at 2.970 μm, Zanchet et al., 2013). In general, this spectral range is affected by the intense and wide absorption of water ice OH centered at ≈3.010 μm (C8, from Mastrapa et al., 2009). The Fresnel peak (C9) is evident in each JIRAM spectra but with some minor shifts of the central wavelength. Again, on orbits 6 and 19, we observe the peak shifted toward shorter wavelengths of about 18 nm for those spectra, possibly as the combined result of different mixing with nonicy materials, relative fractions of crystalline and amorphous forms, or, more likely, surface temperatures. Features C10 to C12 (at 3.300, 3.380, and 3.420 μm, respectively) would be diagnostic of organic matter in both aromatic rings (C10) and aliphatic chains (C11–C12). In general, these features appear very shallow in JIRAM data possibly as a consequence

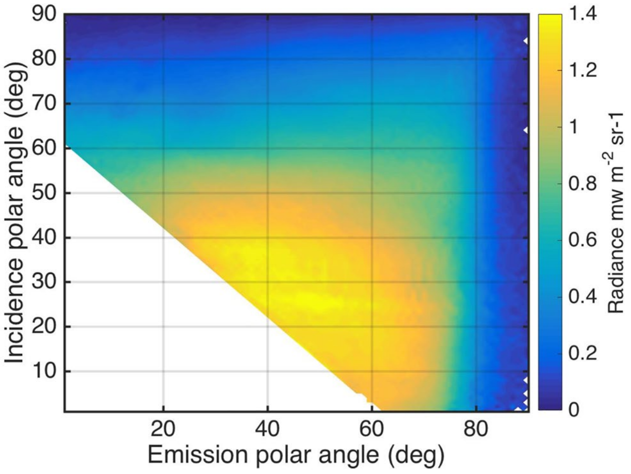

Figure 4. Average radiance from Ganymede surface as a function of emission and incidence angle. Data are from the L-band filter observations during PJ24, and hence radiance is integrated over the 3.3–3.6 μm range. Values for both low-emission/low-incidence angles were not observed in this orbit.

of the low concentrations of these compounds and low instrumental signal-to-noise. The 3.300 μm feature (C10) typical of benzene rings is evident again on orbit 6 and 19 spectra. JIRAM also resolves the signatures characterizing aliphatic organic matter, for example, symmetric and asymmetric stretch modes of CH_2 and CH_3 (Moroz et al., 1998; Sandford et al., 1991): the asymmetric stretch mode of methyl (CH_3) at 3.380 μm (C11), visible on orbit 19 and 24 spectra, appears more intense than the corresponding asymmetric stretch of methylene (CH_2) at 3.420 μm (C12). A similar behavior is not unusual since it has been observed also on comet 67P/Churyumov-Gerasimenko (Raponi et al., 2020). The symmetric modes of CH_2-CH_3 appear blended in the C13 feature at 3.480–3.500 μm (Moroz et al., 1998). This feature is not recognizable in the orbit 19 spectrum. The C13 signature is close to nearby C14 at 3.500 μm where the absorption of radiolytic H_2O_2 is observed and recognized on NIMS spectra by Carlson et al. (1999).

Finally, the spectral range between 4.0 and 4.5 μm (panel D) is affected by the lowest instrumental sensitivity resulting in noisier spectra. Despite these limitations, the feature D16 at 4.260 μm associated with $^{12}CO_2$ in solid state (Quirico et al., 1999; Quirico & Schmitt, 1997; White et al., 2012) appears recurrent in all JIRAM spectra with the exception of orbit 6 where it is absent, and on orbit 19 where it is clearly shifted from 4.260 μm to 4.250 μm. A similar effect is a consequence of the complex bonding/caging of CO_2 with surrounding molecules (Cruikshank et al., 2010) as has been reproduced in the laboratory with experiments of physisorbed and implanted CO_2 in nonice materials (Hibbits & Szanyi, 2007). The shift of the trapped CO_2 band position has been observed on other icy dark surfaces, like Saturn's satellites Iapetus, Hyperion and Phoebe (Filacchione et al., 2010). The orbit 19 spectrum shows two other peculiar features which are not seen in the other spectra: D15 at 4.130 μm is compatible with OD stretch and D17 at 4.380 μm with isotopic $^{13}CO_2$; these two features have been also recently recognized in Cassini VIMS data of CO_2-rich spectra of Saturn's moons Phoebe and Iapetus (Clark et al., 2019).

Within the JIRAM dataset, the peculiar nature of the spectrum from orbit 19 is evident: with a highly deformed 2 μm band, it may be characterized by the minimum abundance of water ice and the maximum abundance of hydrated salts (see features A1, A2, A3), or the result of sulfuric acid hydratation, or the presence of small particles. This spectrum is also the one with the lowest I/F on the continuum at 2.2 μm where typically water ice is very bright (see Figure 3, top-left panel). In contrast with the rest of the JIRAM dataset, both aliphatic symmetric stretch species (C13) and H_2O_2 (C14) seem to be absent in the orbit 19 spectrum.

5. Photometric Model and Surface Reflectance

The unique vantage point of Juno permits JIRAM to observe the same surface element at different illumination and emission angles. This enables testing different photometric corrections, such as the common Lambert model or the Oren and Nayar (1994) model used in Ligier et al. (2019). In the latter approach, photometric correction is expressed as a function of four angles: the solar incidence and emission angles θ_i and θ_e, and the azimuth angles of incidence and emission ϕ_r and ϕ_e. If the surface is isotropic, then only the quantity ϕ_e–ϕ_i matters; θ_i is equal to the solar zenith angle (SZA).

Data from the JIRAM images taken during orbit 24 are more suitable for this analysis than spectroscopic data, as there are more statistics and there is less noise. In Figure 4, we show the average radiance as a function of emission and incidence angle. Data are integrated regardless of the geographical location of the emitting surface element. Hence, in terms of spatial distribution, these data are averaged over about ∼20% of the surface of Ganymede, so we assume that the geographical variability due to bright or dark features is sufficiently smoothed away. Figure 4 shows a clear dependence of the average radiance on both θ_i and θ_e, with an expected cosine law for the first one (solar incidence), and a more subtle, yet similar trend for the emission angle. In the model by Oren and Nayar (1994), which has been used by Ligier et al. (2019) and

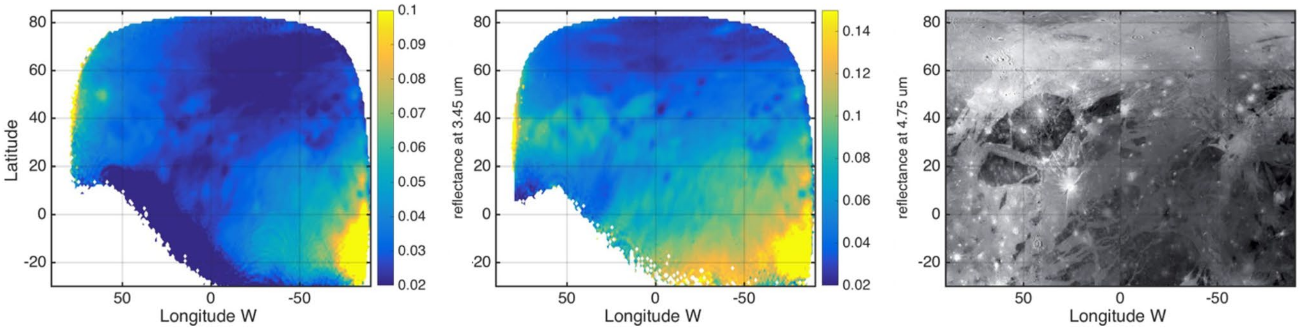

Figure 5. Left: Reflectance at 3.45 μm computed by using all L-band imager data from orbit 24 (averaging over overlapping images) and the photometric model discussed in Section 4; center: same, for the 4.75 μm band (M-band); right: High-resolution image of Ganymede produced by "The Celestia Motherlode": (http://www.celestiamotherlode.net/catalog/jupiter.php) using the USGS Astrogeology Science Center images (http://astrogeology.usgs.gov).

hence is worth discussing here, the Lambert model is improved by taking into account surface roughness (σ). This is obtained by multiplying the Lambert law for a term that depends on σ and is a function of θ_e, θ_i and ϕ_e–ϕ_i. However, this term vanishes when $|\phi_e - \phi_i| > 90°$ (i.e., the photons are scattered in the forward direction once the vectors are projected onto the reflection plane). In our dataset, this is the case for 90% of the observations, and hence their formula turns to a Lambert one and by definition can't fit our observations, which exhibit a dependence on the emission angle. We also note that pixels with very high emission angle could suffer some signal decrease due to the fact that their point-spread-function is partially outside the limb: for this reason, data with emission angle >80° is excluded from the subsequent analysis.

Since the photometric model from Oren and Nayar (1994) cannot be used to fit our data, we produced a simple analytical photometric model by slightly modifying the Lambert cosine law and introducing an explicit dependence on the emission angle:

$$R \sim \left(\cos\theta_i\right)^{c1} \cdot \left(\cos\theta_e\right)^{c2}$$

where *R* is the radiance and *c1* and *c2* are free exponents. By using the data from the L-band imager (orbit 24 only), we obtain $c1 = 1.17$; $c2 = 0.29$. Since the deviation from Lambert's law is not large, we did not recalculate the normalization factor for the new angular distribution, nor did we recalculate the average I/F_c in Figure 2 for both this reason and because the photometric model depends on the wavelength. In fact, it is worth noting that fitting the function with the M-band data would provide different parameters ($c1 = 1.5$ and $c2 = 0.13$). This opens the possibility of performing a future study on the surface properties based on the local variability of the photometric model, considering that the JIRAM dataset includes a large number of observations for most of the surface and covering most emission angles and SZAs.

In Figure 5, we show the average reflectance at 3.45 and 4.75 μm computed by using all imager data (averaging over overlapping images) and the photometric model, that is, dividing by the factor *R* from the equation above. It appears that both the L- and M-band filter reflectance exhibit a general anticorrelation with the albedo distribution at visible wavelengths, both at the global and local scales. In particular, fresh craters, which appear bright in the visible (VIS), have a recognizable low-reflectance counterpart in the infrared (IR) L- and M-band maps. Such behavior would be compatible with the increase of albedo in the VIS due to local water ice enrichment (Carlson et al., 1996), which is bright at these wavelengths. Conversely, longward of 3 μm, the reflectance in the L- and M-band is likely dominated by nonicy opaque material, while water ice is relatively more absorbing and characterized by a low albedo. Such phases would behave as darkening agents at VIS-Near InfraRed wavelengths while being brighter than water ice in the L and M spectral intervals. A decrease of the abundance of the opaque materials (thus corresponding to larger amounts of water ice) in the VIS-bright (IR-dark) areas, may then produce the observed reduction of reflectance in JIRAM L and M data. In this respect, we note that linear spectral modeling from Ligier et al. (2019) in the 1.4–2.5 μm wavelength interval indicates that darkening materials are the dominant compounds on Ganymede's surface (average abundance of 52.8%±12.7%).

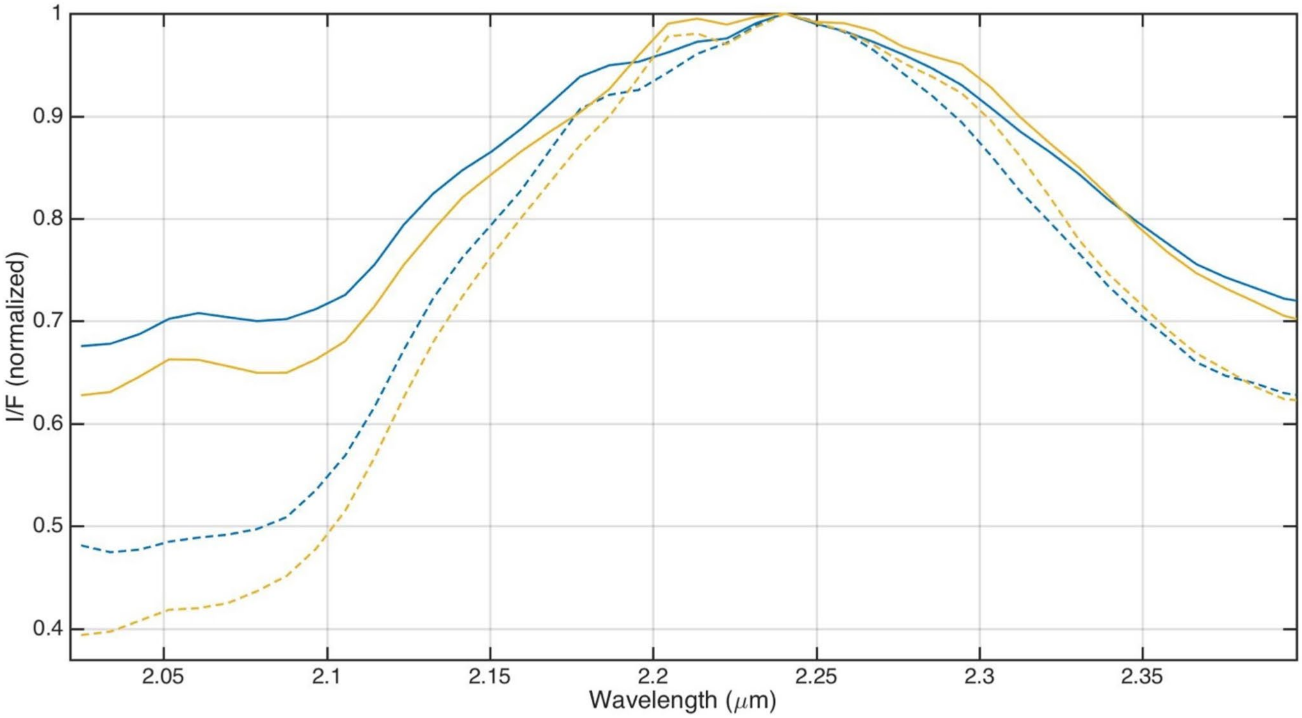

Figure 6. Normalized I/F for the water absorption band at 2 μm. Orange: orbit 6; Blue: orbit 24; dashed line: high latitudes (>45°); solid line: low latitude (<45°). I/F is normalized to its maximum value (at ∼2.25 μm). The absorption strength of the 2 μm water ice absorption band is significantly deeper in high-latitude regions.

When compared to the L-band, the M-band map shows a larger contrast of reflectance between the VIS-bright (IR-dark) spots and the surrounding terrains. This may be ascribed either to the fact that the relative difference in albedo between water ice and the opaque materials is larger in the M-band than in the L-band or to a residual contribution of thermal emission, which, contrary to the L-band, may not be negligible in M-band data. In the latter case, ice-rich areas (VIS-bright, IR-dark) would be characterized by a smaller absorption of solar flux, with decreased surface temperature and thermal emission. This would produce a reduction of radiance in the M-band, with respect to the surrounding warmer ice-poor areas.

6. Distribution of Water Ices

In Figures 6 and 7, we show the normalized I/F for orbits 6 and 24, once the spectra for high and low latitudes have been separated, for the 2-μm water ice absorption band range and the 4.26 μm CO_2 absorption band range respectively. There is a clear distinction in the absorption strength of the 2-μm water ice absorption band, which is significantly deeper, on average, in high-latitude regions. The band depth for water absorption at 2 μm is defined according to Clark and Roush (1984) as:

$$D_b = 1 - \frac{I / F(2\,\mu m)}{I / F(\text{continuum})}$$

For all orbits (except orbit 24, see below), the I/F at 2 μm is calculated as the average of the three spectral channels corresponding to the wavelengths: 2.0292, 2.0382, and 2.0472 μm (we discard the first three spectral channels of JIRAM, which suffer from large calibration residuals). The spectral continuum can be estimated as the average I/F of the three spectral channels, on the right shoulder of the band, corresponding to the wavelengths: 2.236, 2.245, and 2.254 μm. In the calculation of the band depth we assume that the photometric correction is uniform on the very short wavelength range used, which is a first approximation.

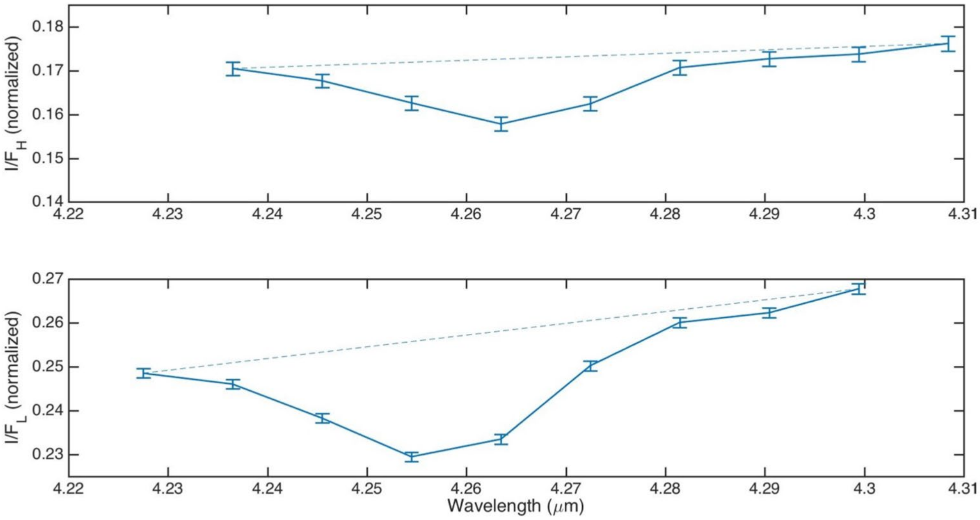

Figure 7. Same as Figure 6 for the CO_2 absorption band at 4.26 μm; only data from orbit 24 are shown. Top: high latitudes; bottom: low latitudes. See text for discussion.

It must be noted that band depth varies when comparing a very wide range of both phase and incident angles (Filacchione et al., 2019); in our observations, taken during flybys, usually the phase angle is uniform during the same flyby, while the incidence angle is very variable; however, comparing band depths from different orbits allows us the identification of this effect. For orbit 24, because of the higher quality of the data, we performed a more accurate processing: each spectrum has been fitted with a function:

$$I\ /\ F(\lambda) = \text{continuum} - \text{band}(\lambda)$$

where the shape of the *band* function is taken by the average I/F (Figure 2) in the range from 2.029 to 2.272 μm. This approach removes spike data, allowing use of almost 30 spectral samples instead of the six mentioned above, and hence increases the SNR. Also, to improve the accuracy on the determination of the emission location for each spectrum, the observation geometry, which is usually reconstructed via SPICE software and data, has been re-processed by using a limb-fitting technique on the images (from the geometry of the images one can reconstruct the geometry of the spectra because intercalibration between the two channels has an uncertainty of less than one pixel, ~0.01°). This is required only for orbit 24, because observations were performed right after a rapid turn of the spacecraft and nutation damping was not complete, so that SPICE-reconstructed geometries have a large uncertainty (up to 0.1°, with larger values at the beginning of the observations).

In Figure 8, we show band depth, D_b, at 2 μm on a equirectangular cylindrical projection for all orbits except orbit 24, while in Figure 9, we show the same for orbit 24 alone. These maps were obtained excluding all spectroscopic data with solar incidence and emission angle values greater than 75°, so as to rule out extreme conditions in terms of both solar illumination (grazing sunlight) and slant angle (warped ground footprints, close to the limb). For orbit 24, considering that the geometry reconstruction is improved, and the spatial resolution is much higher, the limit is relaxed to 85°. We considered a grid with fixed angular resolution of 0.5° both in latitude and in longitude, driven by the best spatial resolution achieved by JIRAM in orbit 24, for example, ~23 km/px. Starting from the geometric information available for the corners of the individual JIRAM pixels, a statistical weight for each ground footprint is defined as the inverse of the projected area, so that data with lower spatial resolution have less weight than data with higher resolution. For each spectral index, for example, depth of the 2.0-μm water ice band, we sum all data with related statistical weight falling within a given bin, then we perform a weighted average keeping track of the overall statistical weight and redundancy. This approach ultimately allows us to provide maps that are truly representative of the spectral indices computed for a single orbit as well as for the entire dataset, despite the broad range of spatial resolutions experienced by JIRAM.

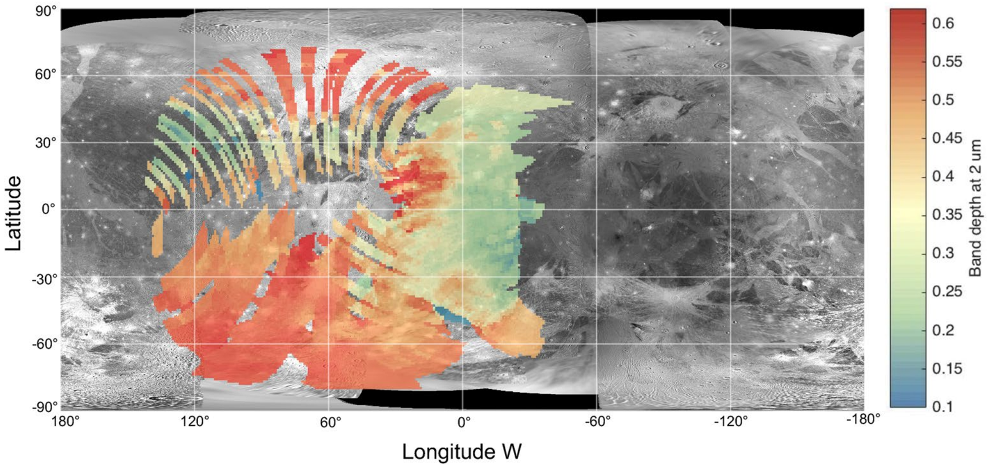

Figure 8. Map of the band depth at 2 μm, obtained by using all JIRAM data except that from orbit 24 (see Figure 9), superimposed over a global image mosaics of Ganymede surface. Red, green, and blue lines are the open/close field lines (OCFL) boundaries for three different configurations: red, when Ganymede is farthest above Jupiter's plasma sheet; green when Ganymede is located in the middle of the plasma sheet; and blue when Ganymede is located farthest below the plasma sheet. Data of OCFL are taken from Khurana et al. (2007). The map is an equirectangular projection with axes scaling chosen to minimize the deformation at 45° latitude. JIRAM, Jovian InfraRed Auroral Mapper.

7. Discussion

The latest, comprehensive works focusing on the distribution of ices on the surface of Ganymede are those of Ligier et al. (2019) and Stephan et al. (2020). In Ligier et al. (2019), data from very large telescope (VLT)/SINFONI (1.40–2.50 μm) are used to produce maps of water ice (total, crystalline, amorphous, small and large grain size), of the darkening agent, of sulfuric acid hydrate, and of chlorinated salts that those authors indicate as the main constituent of nonice material, similar to what they previously found for Europa (Ligier et al., 2016). Because of obvious Earth-based observation constraints, the polar regions are poorly covered as well as the pro-Jovian quadrant, while the observations from Juno nicely complement previous telescopic datasets. Hence, in our study we refer mostly to the results of Ligier et al. (2019).

The geographic distribution and absolute value of D_b is consistent with that of Ligier et al. (2019) and complements that dataset in regions that cannot be covered from Earth. From these images, it appears that the separation region, where the band depth rapidly increases, is located at a latitude of ~45°, matching the position of

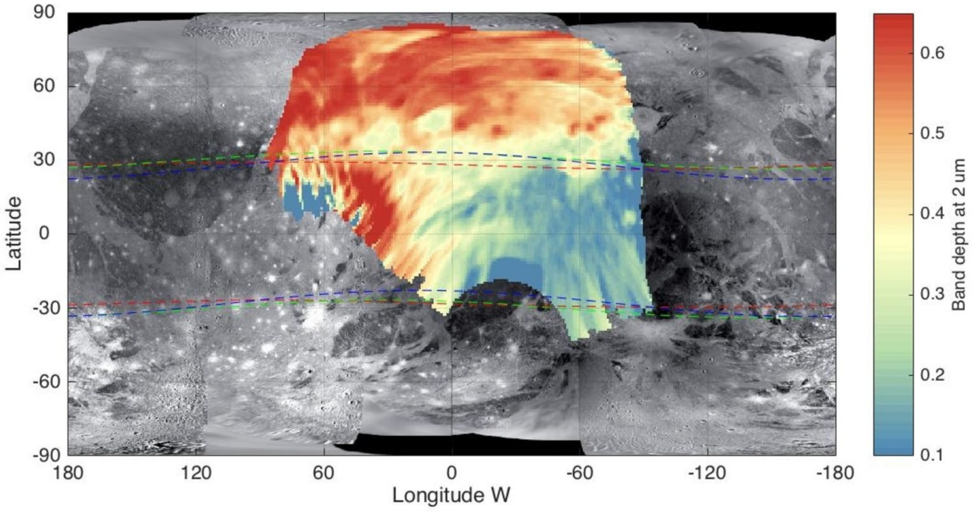

Figure 9. Same as Figure 8, data from orbit 24 only.

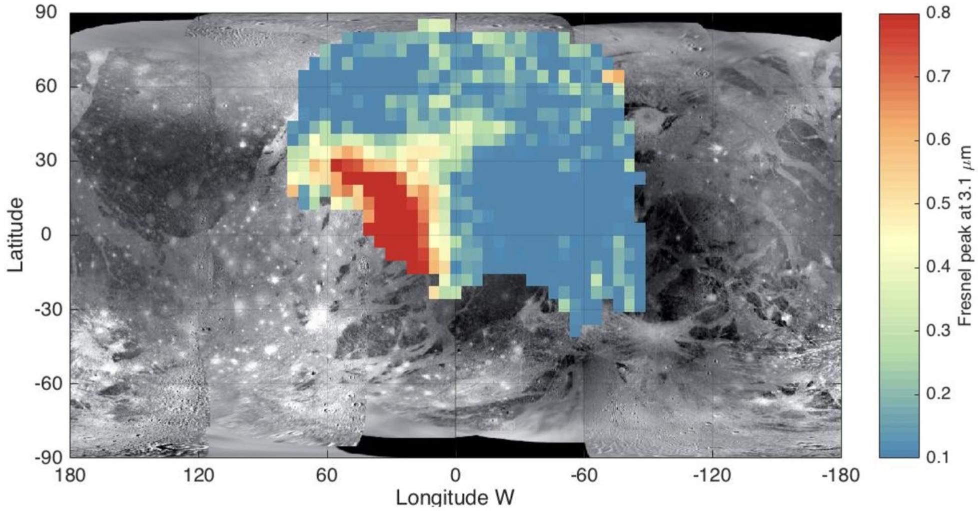

Figure 10. Same as Figure 8, but the intensity of the Fresnel peak of water at 3.1 μm is mapped. Intensity is uncalibrated.

the open-closed magnetic field line boundary. The variations displayed in Figures 8 and 9 further support the aforementioned scenario since they can be ascribed to the abundance of surface ice and possibly to the average size of the water ice grains; however, because some of the spectral features of water ice fall outside of the spectral range of JIRAM, a retrieval of the grain size distribution is not attempted here. There is a significant exception of a very intense absorption region at about 40°W, 20°N; this region roughly corresponds to the area of the 94-km bright rayed crater Tros, centered at 11.14°N, 27.26°W in the leading, pro-Jovian quadrant of Ganymede. This geologically young impact crater, which excavated relatively unweathered subsurface material, shows ejecta features extending up to 10° in specific directions, giving rise to bright terrain. The brighter appearance of the Tros crater area stood out in previous observations obtained by Galileo/NIMS (mosaic 28g005cr) as well as in Ligier et al. (2019), though in telescopic observations the area showing larger band depth values is narrower. One explanation for this apparent discrepancy may be that observations obtained from an orbiting spacecraft span a broader range of geometric conditions. In particular, JIRAM observations are all taken with values of $\phi_e - \phi_i$ greater than 90°, whereas VLT data necessarily have $\phi_e - \phi_i = \sim 0°$.

To further investigate the nature of the bright absorption region in the Tros crater region, we performed a tentative retrieval of the Fresnel reflection peak at 3.1 μm. The shape of the I/F in the 2.8–3.5 μm region is approximated with a Gaussian function centered at 3.1 μm and with 0.050 μm FWHM, plus a second similar Gaussian at 3.2 μm to take into account the deformation of the peak function due to crystalline phase ice (Hansen & McCord, 2004), plus a continuum. Results, in terms of the 3.1 μm peak amplitude, are shown in Figure 10. While water seems ubiquitous with a minor dependence on latitude, the bright Tros crater region is the only clear signature and it shows an extremely high reflection coefficient. Stephan et al. (2020) demonstrated that, using all spectral indices for water ice grain size applied to Galileo/NIMS data with the latest calibration, the average size value on Ganymede varies from 1 μm to 1 mm. The largest H2O grains concentrate at low latitudes and there is a continuous decrease in grain size toward the poles, due to the increasing radiolytic fluxes and consequently an increasingly larger magnitude of sputtering at latitudes greater than 40°. Although crater Tros is not among the local scale features discussed in detail by Stephan et al. (2020), it can be reasonably deduced that the young geological age of the bright terrain associated with Tros and its ejecta, combined with its position in an area relatively protected from the impact of charged particles, can explain a local, larger average size of ice grains compared to surrounding, older terrains.

While the signal in the 2 μm range is well above the noise level and allows an easy fit of the band depth, the spectral radiance longward of 3 μm (and in particular at 4.26 μm—corresponding to the center of the CO_2 band) is very close to the NESR. This complicates mapping the CO_2 band depth, which is only marginally addressed in our study. Instead, we provide the average corrected I/F in the CO_2 range, separately for high and low latitudes (Figure 7). The band depth is 8% for high latitudes and 10% for low latitudes. If we consider that these values are averaged over a large range of latitudes, this is in agreement with results displayed in Figure 11 of Hibbitts et al. (2003), who found a larger amount of CO_2 at lower latitudes. A shift in the center of the CO_2 absorption by one JIRAM spectral channel, from 4.26 μm to 4.25 μm, in principle might be indicative of a different way of CO_2 being trapped in water ice (see Chaban et al., 2007; Cruikshank et al., 2010). The fact that there is a clear difference in the high latitude versus low latitude average spectra in this region is not surprising, but should be analyzed more carefully in a future study. Preliminarily, we note that, unlike on Callisto, impact craters on Ganymede are usually not enriched in CO_2 (Hibbitts et al., 2003). Other preliminary results obtained by Hibbitts et al. () suggested that CO_2 may be concentrated in the moderately hydrated material, primarily associated with the dark regions. However, they pointed out a patchy distribution of CO_2 down to the local scale, arguing that some CO_2-rich impact craters may actually exist on Ganymede.

8. Summary and Conclusions

In this study we presented the first results of JIRAM observations of Ganymede, both imaging and spectral mapping, with a complete coverage of the northern hemisphere and with an average spatial resolution as good as ~25 km. These unique observations enable the study of Ganymede's distinct surface albedo dichotomy between the bright polar caps and the relatively dark equatorial region, pointed out by Smith et al. (1979) and Khurana et al. (2007) and further discussed in later studies (e.g., Plainaki et al., 2015; Poppe et al., 2018). In the following we summarize the main results of our work.

The distribution of water ice for previously unmapped regions has been obtained, both directly from the 2-μm absorption band (obtained from spectral data), and, indirectly, from the comparison between albedo maps at ~3 and ~5 μm (from imager data) with maps in the visible range obtained from the literature. Our data, in summary, confirm that the water ice distribution is compatible with sputtered-induced water ice grain enrichment at high latitude (>45°). Where they overlap, the consistency with previous literature results (Ligier et al., 2019) is good, although some noticeable discrepancies occur, especially close to Tros crater, where we argue that the intensity of the features (in Figures 9 and 10) can be explained by the young geological age of such bright terrain, which implies a larger average size of ice grains compared to surrounding, older terrains. These discrepancies also highlight the importance of a photometric model for Ganymede, which we obtained here, in the IR, for a wide range of different illumination and emission angles. Also, we investigate the latitudinal variability of the 4.26 μm CO_2 absorption band; this shows a moderate variability both in intensity and peak wavelength, which may potentially be indicative of a different way of CO_2 being trapped in water ice. Finally, we have identified, or suggested the identification, of several minor species as discussed in Section 4.

Further analysis of these data may allow an in depth spectral analysis of several surface features, using methodologies and techniques similar to those applied in previous Europa analyses (Filacchione et al., 2019). In principle this will also allow the inference of surface composition (ices and nonice materials), the physical state of the regolith (grain size distribution, ice abundance, and surface temperature) and correlation with morphological features at regional scales.

In view of future space missions that will shed light on the Galilean moons, the feedback to be obtained through the Juno/JIRAM observations (spectral mapping and imaging) could prove fundamental in defining future observation strategies. In particular, the ESA/JUICE mission, which will explore the icy Galilean moons with an emphasis on Ganymede, could greatly benefit from new Ganymede observations acquired by JIRAM. Furthermore, NASA's Europa Clipper mission, while focused on Europa, will likely take advantage of opportunities to make measurements of Ganymede as that spacecraft prepares to settle into its first Europa observation campaign, as well as during subsequent opportunities, also benefitting from the observations with Juno/JIRAM. Because of Juno's mission profile, good observation opportunities for Ganymede will still be feasible in 2020 and 2021. This will result in a large database that, especially for the polar regions, would be unique and not achievable from earth-based observatories.

Data Availability Statement

JIRAM data used in this study is publicly available on the Planetary Data System (http://pds.nasa.gov) and can be downloaded from http://atmos.nmsu.edu:8080/pds. The individual datasets are available at https://atmos.nmsu.edu/ PDS/data/jnojir_xxxx, where xxxx is 1001, 1002, or 1003 for EDR (Experiment

Data Record; raw data) and 2001, 2002, or 2003 for RDR (Reduced Data Record; calibrated data) volumes. Repository for the data products used in this study is: https://doi.org/10.5281/zenodo.4004635

Acknowledgments
JIRAM is funded by the Italian Space Agency (ASI), ASI-INAF contract 2016-23-H.0. Support of the Juno Science and Operations Teams is gratefully acknowledged. Part of this work was supported by the Mainstream INAF project INAF grant 1.05.01.86.11.

References

Acton, C. H. (1996). Ancillary data services of NASA's navigation and ancillary information facility. *Planetary and Space Science*, *44*(1), 65–70.

Adriani, A., Coradini, A., Filacchione, G., Lunine, J. I., Bini, A., Pasqui, C., et al. (2008). JIRAM, the image spectrometer in the near infrared on board the Juno mission to Jupiter. *Astrobiology*, *8*(3), 613–622. https://doi.org/10.1089/ast.2007.0167

Adriani, A., Filacchione, G., Di Iorio, T., Turrini, D., Noschese, R., Cicchetti, A., et al. (2014). JIRAM, the Jovian Infrared Auroral Mapper. *Space Science Reviews*, *213*, 393–446. https://doi.org/10.1007/s11214-014-0094-y

Adriani, A., Moriconi, M. L., Mura, A., Tosi, F., Sindoni, G., Noschese, R., et al. (2016). Juno's earth flyby: The Jovian Infrared Auroral Mapper preliminary results. *Astrophysics and Space Science*, *361*(8), 272. https://doi.org/10.1007/s10509-016-2842-9

Bolton, S. J., Adriani, A., Adumitroaie, V., Allison, M., Anderson, J., Atreya, S., et al. (2017). Jupiter's interior and deep atmosphere: The initial Pole-to-Pole passes with the Juno spacecraft. *Science*, *26*, 821–825.

Calvin, W. M., Clark, R. N., Brown, R. H., & Spencer, J. R. (1995). Spectra of the icy Galilean satellites from 0.2 to 5 μm: A compilation, new observations, and a recent summary. *Journal of Geophysical Research*, *100*(9), 19041–19048.

Carlson, R. W., Anderson, M. S., Johnson, R. E., Smythe, W. D., Hendrix, A. R., Barth, C. A., et al. (1999). Hydrogen peroxide on the surface of Europa. *Science*, *283*(5410), 2062–2064.

Carlson, R., Smythe, W., Baines, K., Barbinis, E., Becker, K., Burns, R., et al. (1996). Near-infrared spectroscopy and spectral mapping of Jupiter and the Galilean satellites: Results from Galileo's initial orbit. *Science*, *274*(5286), 385–388.

Carlson, R. W., Weissman, P. R., Smythe, W. D., & Mahoney, J. C. (1992). Near-infrared mapping spectrometer experiment on Galileo. *Space Science Reviews*, *60*, 457–502.

Chaban, G. M., Bernstein, M., & Cruikshank, D. P. (2007). Carbon dioxide on planetary bodies: Theoretical and experimental studies of molecular complexes. *Icarus*, *187*(2), 592–599.

Clark, R. N., Brown, R. H., Jaumann, R., Cruikshank, D. P., Nelson, R. M., Buratti, B. J., et al. (2005). Compositional maps of Saturn's moon Phoebe from imaging spectroscopy. *Nature*, *435*(7038), 66–69.

Clark, R. N., Curchin, J. M., Jaumann, R., Cruikshank, D. P., Brown, R. H., Hoefen, T. M., et al. (2008). Compositional mapping of Saturn's satellite Dione with Cassini VIMS and implications of dark material in the Saturn system, *Icarus*, *193*(2), 372–386.

Clark, R. N., Cruikshank, D. P., Jaumann, R., Brown, R. H., Stephan, K., Dalle Ore, C. M., et al. (2012). The surface composition of Iapetus: Mapping results from Cassini VIMS. *Icarus*, *218*, 831–860. https://doi.org/10.1016/j.icarus.2012.01.008

Clark, R. N., Brown, R. H., Cruikshank, D. P., Swayze, G. A. (2019). Isotopic ratios of Saturn's rings and satellites: Implications for the origin of water and Phoebe. *Icarus*, *321*, 791–802.

Clark, R. N., & McCord, T. B. (1980). The Galilean satellites: New near- infrared spectral reflectance measurements (0.65 – 2.5 mm) and a 0.325 – 5 μm summary. *Icarus*, *41*, 323–339.

Clark, R. N., & Roush, T. L. (1984). Reflectance spectroscopy: Quantitative analysis techniques for remote sensing applications. *Journal of Geophysical Research*, *89*(B7), 6329–6340.

Cruikshank, D. P., Meyer, A. W., Brown, R. H., Clark, R. N., Jaumann, R., Stephan, K., et al. (2010). Carbon dioxide on the satellites of Saturn: Results from the Cassini VIMS investigation and revisions to the VIMS wavelength scale. *Icarus*, *206*, 561–572.

Cruikshank, D. P., Moroz, L., & Clark, R. N. (2020). Chapter 5: Visible and infrared spectroscopy of ices, volatiles and organics. In J. L. Bishop, J. F. BellIII, & J. E. Moersch (Eds.), *Remote compositional analysis: Techniques for understanding spectroscopy, mineralogy, and geochemistry of planetary surfaces* (pp. 102–119). Cambridge, UK: Cambridge University Press. https://doi.org/10.1017/9781316888872

Dalton, J. B., & Pitman, K. M. (2012). Low temperature optical constants of some hydrated sulfates relevant to planetary surfaces. *Journal of Geophysical Research*, *117*(E9), E09001. https://doi.org/10.1029/2011JE004036.

De Angelis, S., Carli, C., Tosi, F., Beck, P., Schmitt, B., Piccioni, G., et al. (2017). Temperature-dependent VNIR spectroscopy of hydrated Mg-sulfates. *Icarus*, *281*, 444–458.

Filacchione, G., Capaccioni, F., Clark, R. N., Cuzzi, J. N., Cruikshank, D. P., Coradini, A., et al. (2010). Saturn's icy satellites investigated by Cassini-VIMS. II. Results at the end of nominal mission. *Icarus*, *206*, 507–523.

Filacchione, G., Adriani, A., Mura, A., Tosi, F., Lunine, J., Raponi, A., et al. (2019). Serendipitous infrared observations of Europa by Juno/JIRAM. *Icarus*, *328*, 1–13.

Grasset, O., Castillo-Rogez, J., Guillot, T., Fletcher, L. N., & Tosi, F. (2017). Water and volatiles in the outer solar system. *Space Science Reviews*, *212*, 835–875.

Grundy, W. M., Buratti, B. J., Cheng, A. F., Emery, J. P., Lunsford, A., McKinnon, W. B., et al. (2007). New Horizons mapping of Europa and Ganymede. *Science*, *318*, 234. https://doi.org/10.1126/science.1147623

Hansen, G. B., & McCord, T. B. (2004). Amorphous and crystalline ice on the Galilean satellites: A balance between thermal and radiolytic processes. *Journal of Geophysical Research*, *109*, E01012, https://doi.org/10.1029/2003JE002149

Hapke, B. (1993). *Theory of reflectance and emittance spectroscopy*. Cambridge, UK: Cambridge University Press.

Hibbitts, C. A., & Szanyi, J., (2007). Physisorption of CO_2 on non-ice materials relevant to icy satellites, *Icarus*, *191*, 371–380.

Hibbitts, C. A., Pappalardo, R. T., Hansen, G. B., & McCord, T. B. (2003). Carbon dioxide on Ganymede. *Journal of Geophysical Research*, *108*(5), 5036. https://doi.org/10.1029/2002JE001956.

Jia, X., Walker, R. J., Kivelson, M. G., Khurana, K. K., & Linker, J. A. (2009). Properties of Ganymede's magnetosphere inferred from improved three-dimensional MHD simulations. *Journal of Geophysical Research*, *114*, A09209. https://doi.org/10.1029/2009JA014375

Johnson, T. V., Yeates, C. M., & Young, R. (1992). Space science reviews volume on Galileo mission overview. In C. T. Russell (Ed.), *The Galileo mission*. Dordrecht: Springer.

Khurana, K. K., Pappalardo, R. T., Murphy, N., & Denk, T. (2007). The origin of Ganymede's polar caps. *Icarus*, *191*, 193–202. https://doi.org/10.1016/j.icarus.2007.04.022

Kieffer, H. H., & Smythe, W. D. (1974). Frost spectra: Comparison with Jupiter's satellites. *Icarus*, *21*, 506–512.

Kivelson, M. G., Khurana, K. K., Russell, C. T., Walker, R. J., Warnecke, J., Coroniti, F. V., et al. (1996). Discovery of Ganymede's magnetic field by the Galileo spacecraft. *Nature*, *384*, 537–541. https://doi.org/10.1038/384537a0

Kuiper, G. P. (1957). Infrared observations of planets and satellites (abstract). *The Astronomical Journal*, *62*, 245.

Kuiper, G. P. (1961). Limits of completeness. In G. P. Kuiper, & B. M. Middlehurst (Eds.), *Planets and satellites* (pp. 575–591). Chicago, IL: University of Chicago Press.

Kurucz, R. L. (1995). The solar irradiance by computation; in Proceedings of the 17th Annual Conference on atmospheric Transmission models, PL-TR-95-2060. In G. P. Anderson, R. H. Picard, & J. H. Chetwind (Eds.), *Phillips Laboratory Directorate of Geo-physics, Hanscom Air Force Base, Mass., 1995* (pp. 333–334). Retrieved from https://www.nrel.gov/grid/solar-resource/spectra.html#paneld10e138_1

Kurucz, R. L. (2005). Solar spectrum obtainable in MODTRAN 5.2.1. Retrieved from http://kurucz.harvard.edu/sun.html

Leblanc, F., Oza, A. V., Leclerq, L., Schmidt, C., Cassidy, T., Modolo, R., et al. (2017). On the orbital variability of Ganymede's atmosphere. *Icarus*, *293*, 185–198.

Ligier, N., Paranicas, C., Carter, J., Poulet, F., Calvin, W. M., Nordheim, T. A.&, et al. (2019). Surface composition and properties of Ganymede: Updates from ground-based observations with the near-infrared imaging spectrometer SINFONI/VLT/ESO. *Icarus*, *333*, 496–515.

Ligier, N., Poulet, F., Carter, J., Brunetto, R., & Gourgeot, F. (2016). *The Astronomical Journal*, *151*, 163.

Mastrapa, R. M., Bernstein, M. P., Sandford, S. A., Roush, T. L., Cruikshank, D. P., & Dalle Ore, C. M. (2008). Optical constants of amorphous and crystalline H2O-ice in the near infrared from 1.1 to 2.6 μm. *Icarus*, *197*, 307–320.

Mastrapa, R. M., Sandford, S. A., Roush, T. L., Cruikshank, D. P., & Dalle Ore, C. M. (2009). Optical constants of amorphous and crystalline H2O-ice: 2.5-22 μm (4000-455 cm-1) optical constants of H2O-ice. *Acta Pathologica Japonica*, *701*, 1347–1356.

McCord, T. B., Carlson, R. W., Smythe, W. D., Hansen, G. B., Clark, R. N., Hibbitts, C. A., et al. (1997). Organics and other molecules in the surfaces of Callisto and Ganymede. *Science*, *278*, 271–275.

McCord, T. B., Hansen, G. B., & Hibbitts, C. A. (2001). Hydrated salt minerals on Ganymede's surface: Evidence of an ocean below. *Science*, *292*(5521), 1523–1525. https://doi.org/10.1126/science.1059916

McCord, T. B., Coradini, A., Hibbitts, C. A., Capaccioni, F., Hansen, G. B., Filacchione, G., et al. (2004). Cassini VIMS observations of the Galilean satellites including the VIMS calibration procedure. *Icarus*, *172*, 104–126.

McCord, T. B., Hansen, G. B., Clark, R. N., Martin, P. D., Hibbitts, C. A., Fanale, F. P., et al. (1998). Non-water ice constituents in the surface material of the icy Galilean satellites from the Galileo near-infrared mapping spectrometer investigation. *Journal of Geophysical Research*, *103*(E4), 8603–8626.

McCord, T. B., Hansen, G. B., Matson, D. L., Jonhson, T. V., Crowley, J. K., Fanale, F. P., et al. (1999). Hydrated salt minerals on Europa's surface from the Galileo near- infrared mapping spectrometer (NIMS) investigation. *Journal of Geophysical Research*, *104*, 11827–11852.

Moroz, V. I. (1965). Infrared spectrophotometry of the moon and the Galilean satellites of Jupiter. *Soviet Astronomy*, *9*, 999–1006.

Moroz, L. V., Arnold, G., Korochantsev, A. V., & Wäsch, R. (1998). Natural solid bitumens as possible analogs for cometary and asteroid organics:. 1. Reflectance spectroscopy of pure bitumens. *Icarus*, *134*, 253–268.

Mura, A., Adriani, A., Tosi, F., Lopes, R. M. C., Sindoni, G., Filacchione, G. (2020a). Infrared observations of Io from Juno. *Icarus*, *341*, 113607. https://doi.org/10.1016/j.icarus.2019.113607

Mura, A. (2020b). Repository: Data for the research article: "Infrared observations of Ganymede from Juno/JIRAM". Retrieved from https://doi.org/10.5281/zenodo.4004635

Oren, M., & Nayar, S. K. (1994). Generalization of Lambert's Reflectance Model. SIGGRAPH '94: Proceedings of the 21st Annual Conference on Computer Graphics and Interactive Techniques, pp. 239–246. https://doi.org/10.1145/192161.192213

Pappalardo, R. T., Collins, G. C., Head, J. W., III, Helfenstein, P., McCord, T. B., Moore, J. M., et al. (2004). Geology of Ganymede. In F. Bagenal, T. Dowling, & W. McKinnon (Eds.), *Jupiter* (pp. 363–396). Cambridge, UK: Cambridge University Press.

Paty, C., Paterson, W., & Winglee, R. (2008). Ion energization in Ganymede's magnetosphere: Using multifluid simulations to interpret ion energy spectrograms. *Journal of Geophysical Research*, *113*, A06211. https://doi.org/10.1029/2007JA012848

Plainaki, C., Milillo, A., Massetti, S., Mura, A., Jia, X., Orsini, S., et al. (2015). The H2O and O2 exospheres of Ganymede: The result of a complex interaction between the Jovian magnetospheric ions and the icy moon. *Icarus*, *245*, 306–319. https://doi.org/10.1016/j.icarus.2014.09.018

Plainaki, C., et al. (2018). Kinetic simulations of the Jovian energetic ion circulation around Ganymede. *The Astrophysical Journal*, *900*(1), 74. https://doi.org/10.3847/1538-4357/aba94c

Pollack, J. B., Witteborn, F. C., Erickson, E. F., Strecker, D. W., Baldwin, B. J., & Bunch, T. E. (1978). Near-infrared spectra of the Galilean satellites: Observations and compositional implications. *Icarus*, *36*, 271–303.

Poppe, A. R., Fatemi, S., & Khurana, K. K. (2018). Thermal and energetic Ion dynamics in Ganymede's magnetosphere. *Journal of Geophysical Research: Space Physics*, *123*, 4614–4637. https://doi.org/10.1029/2018JA025312.

Quirico, E., Douté, S., Schmitt, B., de Bergh, C., Cruikshank, D. P., Owen, T. C., et al. (1999). Composition, physical state, and distribution of ices at the surface of Triton. *Icarus*, *139*, 159–178.

Quirico, E., & Schmitt, B. (1997). Near-infrared spectroscopy of simple hydrocarbons and carbon oxides diluted in solid N2 and as pure ices: Implications for Triton and Pluto. *Icarus*, *127*, 354–378.

Raponi, A., Ciarniello, M., Capaccioni, F., Mennella, V., Filacchione, G., & Vinogradoff, V., et al. (2020). Infrared detection of aliphatic organics on a cometary nucleus. *Nature Astronomy , 4, 500–505*. https://doi.org/10.1038/s41550-019-0992-8

Sandford, S. A., Allamandola, L. J., Tielens, A. G. G. M., Sellgren, K., Tapia, M., & Pendleton, Y. (1991). The Interstellar C-H stretching band near 3.4 microns: Constraints on the composition of organic material in the diffuse interstellar medium. *Acta Pathologica Japonica*, *371*, 607.

Schubert, G., Anderson, J. D., Spohn, T., & McKinnon, W. B. (2004). Interior composition, structure and dynamics of the Galilean satellites. In F. Bagenal, T. E. Dowling, & W. B. McKinnon (Eds.), Jupiter. The planet, satellites and magnetosphere, Cambridge planetary science. (Vol. 1, pp. 281–306). Cambridge, UK: Cambridge University Press.

Sill, G. T., & Clark, R. N. (1982). Composition of the surfaces of the Galilean satellites. In D. Morrison (Ed.), *Satellites of Jupiter* (pp. 174–212). Tucson: University of Arizona Press.

Smith, B. A., Soderblom, L. A., Beebe, R., Boyce, J., Briggs, G., Carr, M., et al. (1979). The Galilean satellites and Jupiter: Voyager 2 imaging science results. *Science*, *206*(4421), 927–950.

Spencer, J. R. (1986). Icy Galilean satellite reflectance spectra: Less ice on Ganymede and Callisto? *Icarus*, *70*, 99–110.

Stephan, K., Hibbitts, C. A., & Jaumann, R. (2020). H2O-ice particle size variations across Ganymede's and Callisto's surface. *Icarus*, *337*, 113440.

Thompson, D. R., Seidel, F. C., Gao, B. C., Gierach, M. M., Green, R. O., Kudela, R. M., & Mouroulis, P. (2015). Optimizing irradiance estimates for coastal and inland water imaging spectroscopy. *Geophysical Research Letters*, *42*, 4116–4123. https://doi.org/10.1002/2015GL063287

Tosi, F., Mura, A., Lopes, R. M. C., Filacchione, G., Ciarniello, M., Zambon, F., et al. (2020). Mapping Io's surface composition with Juno/JIRAM. *Journal of Geophysical Research: Planets*. https://doi.org/10.1029/2020JE006522

White, D. W., Mastrapa, R. M., & Sandford, S. (2012). Laboratory spectra of CO_2 vibrational modes in planetary ice analogs. *Icarus*, *221*, 1032–1042.

Zanchet, A., Rodrıguez-Lazcano, Y., Galvez, O., Herrero, V. J., Escribano, R., & Mate, B. (2013). Optical constants of NH3 and NH3:N2 amorphous ices in the near-infrared and mid-infrared regions. *Acta Pathologica Japonica*, *777*(26), 11.